Separation and Purification Technology 360 (2025) 131212

Contents lists available at ScienceDirect

Separation and Purification Technology

journal homepage: www.elsevier.com/locate/seppur

CFD insights into microwave- assisted deep eutectic solvent for the recovery of astaxanthin from bacteria *Paracoccus carotinifaciens*: From extraction to agricultural applications

Cassamo U. Mussagy [a,*], Angie V. Caicedo Paz [a], Pablo Cornejo [b], Christian Santander [c], Felipe González [d], Rafael G. Voloua [a,1], Ximena Besoain [a,e], Alejandra Larach [a], Aldo Salinas [a], Karina Godoy [f], Diakaridia Sangaré [g,*]

[a] *Escuela de Agronomía, Facultad de Ciencias Agronómicas y de los Alimentos, Pontificia Universidad Católica de Valparaíso, Quillota 2260000, Chile*
[b] *Centro de Estudios Avanzados en Fruticultura (CEAF), Rengo 2940000, Chile*
[c] *Departamento de Ciencias Químicas y Recursos Naturales, Scientific and Technological Bioresource Nucleus BIOREN-UFRO, Universidad de La Frontera, Temuco 4811230, Chile*
[d] *Programa de Doctorado en Ciencias Mención Biología Celular y Molecular Aplicada, Facultad de Ciencias Agropecuarias y Medioambiente, Universidad de La Frontera, Temuco 4811230, Chile*
[e] *Núcleo Milenio Bioproductos, Genómica y Microbiología Ambiental—BioGEM, Chile*
[f] *Center of Plant–Soil Interaction and Natural Resources Biotechnology, Scientific and TechnologicalBioresource Nucleus (BIOREN-UFRO), Universidad de La Frontera, Avenida Francisco Salazar 01145, P.O. Box 54-D, Temuco 4780000, Chile*
[g] *CIRAD, UPR BioWooEB, 73 rue Jean-François Breton, F-34398 Montpellier, France*

A R T I C L E I N F O

Editor: Raquel Aires Barros

Keywords:
Zero-waste biorefinery
Paracoccus carotinifaciens
Astaxanthin
CFD
Microwave-assisted deep eutectic solvents
Antifungal activity
Biofertilizer applications

A B S T R A C T

Biorefineries are at the forefront of sustainable innovation, extracting and processing bioactive compounds from microorganisms and other biological sources for various applications in agriculture and food production. Among these compounds, astaxanthin (AXT) stands out for its remarkable antioxidant properties and significant health benefits. This study introduces a pioneering approach to developing a zero-waste, bacterial-based biorefinery by using microwave (MW)-assisted deep eutectic solvents (DES) for the extraction of astaxanthin-rich extracts (ARE) from *Paracoccus carotinifaciens*. Computational Fluid Dynamics (CFD) simulations was used to study the MW-ARE extraction process by accurately modeling the flow and mixing behaviors of DES during MW extraction, as well as the heat and mass transfer within the system. The DES enriched with ARE was thoroughly tested for their antifungal and anti-oomycete activity against *Botrytis cinerea* and *Phytophthora cinnamomi*, respectively, taking advantage of the high antioxidant and antimicrobial properties of ARE. Additionally, the remaining colorless fraction of *P. carotinifaciens* left after MW-ARE extraction was repurposed as a biofertilizer to enhance the growth of lettuce plants (*Lactuca sativa* L.). This comprehensive study provides a valuable insight into the mechanisms of ARE recovery using MW-assisted extraction and lay the groundwork for a robust, efficient, and sustainable biorefinery model that minimizes waste and maximizes the use of bacterial biomass, aligning with the principles of a circular economy, to elevate product quality and promote sustainable agricultural practices.

1. Introduction

Biorefineries are specialized facilities that extract and process bioactive compounds from microorganisms and other biological sources [1–3]. These compounds, including natural antioxidants and other functional compounds, have diverse applications in pharmacy, agriculture, and food production [4]. By applying these bioactive compounds, biorefineries "open door" to improved product quality, enhanced nutritional value, and sustainable practices [5]. Additionally, they support the principles of a circular economy by maximizing resource efficiency, minimizing waste, and promoting the reuse and recycling of materials [6–8]. Among bioactive compounds, astaxanthin

* Corresponding authors.
E-mail addresses: cassamo.mussagy@pucv.cl (C.U. Mussagy), diakaridia.sangare@cirad.fr (D. Sangaré).
[1] *In memoriam* Dr(c) Rafael G. Voloua.

https://doi.org/10.1016/j.seppur.2024.131212
Received 4 November 2024; Received in revised form 17 December 2024; Accepted 19 December 2024
Available online 21 December 2024

(AXT) is notable for its powerful antioxidant properties [9,10]. As one of the most potent antioxidants in the carotenoid family, AXT is recognized for its deep red color and significant health benefits, including its ability to reduce oxidative stress and protect against cellular damage [11]. AXT can be sourced from three main natural sources: microalgae, yeast, and bacteria [12]. While microalgae and yeast are more commonly used, bacterial sources are increasingly recognized for their advantages. Specifically, the bacterial cell wall, which consists of a thin peptidoglycan layer [9], facilitates a simple and efficient extraction process, yielding high quantities of AXT. *Paracoccus carotinifaciens* is a gram-negative bacterium that produces natural AXT in a *trans*-free form, with AXT making up nearly 70–80 % of carotenoid composition [13]. Most commercially available AXT is synthetic or derived from microalgae (i.e., *Haematococcus pluvialis*) which typically yields about 80 % esterified AXT [14,15]. Using *P. carotinifaciens* biomass, which is already commercially available and has a well-established industrial production process, as a new source of natural AXT could provide AXT unique quality. This fact opens opportunities to explore its diverse functions, benefits, and potential applications.

AXT is produced intracellularly in *P. carotinifaciens*, requiring effective extraction methodologies for successful recovery [16]. Conventional methods, such as stirring, heat-assisted extraction, and maceration, have been commonly employed [17]. In contrast, non-conventional methods like ultrasound-assisted and microwave (MW) extraction have emerged as efficient alternatives [16]. MW, often called as “green technology,” is praised for its high efficiency, reduced solvent usage, and lower environmental impact [18–20]. This method contrasts with conventional approaches, which typically involve multiple steps that can lead to product loss, contamination, longer processing times, and environmental issues [21,22]. It is important to note that while the thin bacterial cell wall can facilitate AXT recovery, the effectiveness of AXT extraction depends on the solvent used and the affinity between the solvent and hydrophobic AXT. Common volatile organic compounds (VOCs) used for AXT extraction include acetone, chloroform, hexane, and methanol [16]. However, some of these solvents are known to harm both the environment and human health, raising concerns for large-scale industrial processes and their sustainability [23]. Non-conventional extraction methods that utilize less toxic solvents, including Deep Eutectic Solvents (DES) [24,25]. DES are merging to address these issues and are considered a promising alternative due to their low toxicity and biodegradability [26].

Tailor-made hydrophobic DES have been tested with various non-polar carotenoids [27]. In our previous work on recovering astaxanthin-rich extracts (ARE) from *P. carotinifaciens*, nearly 150 mg/mL of ARE was obtained using ultrasound-assisted extraction with a DES composed of choline chloride [Ch]Cl as the hydrogen bond acceptor and acetic acid (AA) (at 1:3 M ratio) as the hydrogen bond donor [16]. This highlights the efficiency of DES in the AXT extraction process. However, purifying ARE after extraction with DES poses challenges, such as difficulty separating AXT from the DES due to low vapor pressures and high viscosity [28]. One potential solution is to explore DES rich in ARE applications for antifungal and anti-oomicete purposes, utilizing both the properties of DES and the beneficial effects of AXT.

Given the potential of DES ([Ch]Cl: AA (1:3)), it is crucial to investigate further other non-conventional extraction technologies, such as MW-assisted extraction, to enhance the recovery of intracellular ARE from *P. carotinifaciens*. MW-assisted extraction could improve the efficiency of ARE extraction by intensifying the process and overcoming some of the limitations associated with traditional methods and DES. Furthermore, incorporating Computational Fluid Dynamics (CFD) can provide a deeper understanding of the mechanisms involved in the MW-assisted extraction of ARE. CFD can model DES's flow and mixing behaviors during MW extraction, visualizing how DES interacts with *P. carotinifaciens* cells. This fact provides insights into how effectively the DES permeabilizes the cell wall and solubilizes the intracellular ARE under different operating conditions, such as temperature, MW potency, and solvent/biomass ratios. Additionally, CFD can simulate heat and mass transfer within the extraction system, aiding in the design of more efficient and sustainable processes [29,30].

Considering the outlined background, this study aims to develop a zero-waste, bacterial-based biorefinery utilizing MW-assisted DES extraction to recover ARE from *P. carotinifaciens*. To optimize the process, CFD simulations were performed to evaluate the influence of operational parameters on the efficiency of ARE recovery. The resulting ARE-enriched DES was tested for its antifungal activity against *Botrytis cinerea* and *Phytophthora cinnamomi*, pathogens of significant agricultural importance. The high antioxidant and antimicrobial properties of ARE were expected to enhance the efficacy of these extracts in controlling fungal growth. Additionally, the colorless biomass fraction of *P. carotinifaciens*, remaining after MW-assisted ARE extraction, was utilized as a biofertilizer to promote the growth of lettuce plants (*Lactuca sativa* L.). This integrated approach not only provides valuable insights into the mechanisms of MW-assisted ARE extraction but also establishes a sustainable and efficient biorefinery model that maximizes the utilization of bacterial biomass while minimizing waste generation.

2. Materials and methods

2.1. Chemical and reagents

High-purity (*all-E*)-astaxanthin standard choline chloride $\geq$ 98 % and acetic acid ($\geq$99.5 %), were purchased from Sigma-Aldrich (St. Louis, MO, USA). All other reagents incorporated in the experiment were of high purity, with levels greater than or equal to 99 %, and were utilized directly without undergoing any additional purification processes. DESs were prepared by combining choline chloride ([Ch]Cl) as the HBA and acetic acid (AA) as the HBD at a 1:3 M ratio. The mixture was heated to 80 °C under constant stirring until a clear liquid phase was achieved. After reaching this point, the solution was allowed to cool to room temperature before being utilized in solid–liquid extraction.

2.2. Biological sample

The microbial biomass employed in this study to obtain ARE was obtained from *Paracoccus carotinifaciens*, a Gram-negative bacterium originating from a marine habitat. $CaCO_3$ was used as an excipient in the stabilization process of bacterial biomass during preservation. The carotenoid-concentrated dried biomass of *P. carotinifaciens* (Panaferd-AX) was generously supplied by the ENEOS group (Tokyo, Japan) as a gift.

2.3. ARE solid–liquid extraction

The SLE of ARE was conducted using a 250 mL spherical flask reactor containing 50 mL of DES and 1 g of *P. carotinifaciens* biomass. The extraction was performed on a commercial microwave (MW) Midea model MMP (Santiago de Chile, Chile) coupled with a thermocouple and magnetic stirrer. MW can be operated at various power levels up to 1000 W for 200 s min at different potency (from 300 to 500 W), depending on the experimental procedure described in the next sections. The samples were then centrifuged using an Orto Alresa Minicen centrifuge (Madrid, Spain) at 2500 *x*g and 25 °C for 6 min. After centrifugation, the supernatants rich in ARE were carefully collected, avoiding light exposure, and stored for subsequent analysis of ARE content. The ARE content was determined following the method described by Caicedo-Paz et al. [16].

2.3.1. Microwave geometric modeling

The proposed MW system in this study consists of a modified domestic MW oven, a metal enclosure connected to a 2.45 GHz wave source through a rectangular waveguide, operating in transverse electric mode (TE_{10}). A cylindrical glass plate (glass tray) inside the oven is

placed at the bottom, with a spherical flask extraction sample at the top. The microwaves can be operated at various power levels up to 1000 W. Fig. 1 shows the complete geometry of the microwave system.

The rectangular port is excited by a transverse electric (TE) wave, which lacks an electric field component in the propagation direction. At an excitation frequency of 2.45 GHz, the only mode that can propagate through the rectangular waveguide is the TE_{10} mode [31]. The cutoff frequencies for the different modes are given analytically based on their corresponding relationships.

$$(\nu_c)_{mn} = \frac{c}{2}\sqrt{\left(\frac{m}{a}\right)^2 + \left(\frac{n}{b}\right)^2} \tag{1}$$

where c is the speed of light, and a and b are the waveguide dimensions. For the TE_{10} mode, m=1 and n = 0, a and b are the dimensions of the waveguide rectangular cross-section (a = 7.8 cm and b = 1.8 cm). The port condition requires a propagation constant β. This constant β can be expressed as a function of the frequency ν and the waveguide dimensions. The general formula for β in a rectangular waveguide is:

$$\beta = \sqrt{{k_0}^2 - \left(\frac{m\pi}{a}\right)^2 - \left(\frac{n\pi}{b}\right)^2} \tag{2}$$

where k_0 is the wavenumber in vacuum and is:

$$k = 2\pi\nu_c \tag{3}$$

2.3.2. Electromagnetic field modeling

Maxwell's equations were used in different contexts to model the energy distribution in the oven and the product [32,33]. Inside the oven, microwaves propagate and reflect off the walls, creating an electric and magnetic (Electromagnetic) field that varies in space.

$$\nabla \times {\mu_r}^{-1}(\nabla \times E) - {k_0}^2(\varepsilon_{rc})E = 0 \tag{4}$$

where E is the electric field intensity, ε_{rc} is the complex dielectric permittivity, and μ_r is the magnetic permeability.

$$\varepsilon_{rc} = \varepsilon' - j\epsilon'' \tag{5}$$

$$k_0 = \frac{2\pi f}{c}\sqrt{\frac{\varepsilon'\left(\sqrt{(1+tan^2\delta)}+1\right)}{2}} + i\frac{2\pi f}{c}\sqrt{\frac{\varepsilon'\left(\sqrt{(1+tan^2\delta)}-1\right)}{2}} \tag{6}$$

$$tan(\delta) = \frac{\epsilon''}{\varepsilon'} \tag{7}$$

where ϵ' represents the dielectric constant, which is the real part of the dielectric permittivity. It indicates how much a material can store electrical energy in an electric field; ϵ'' is the loss factor, indicating how much of that energy is dissipated as heat, affecting heating efficiency; f is the microwave frequency, and tan(δ) is the loss tangent [32]. In the boundary condition:

$$n \times E = 0 \tag{8}$$

This equation ensures that the electric field meets the boundary conditions at the system surfaces. This issue is important in determining how electromagnetic waves interact with the oven boundaries, ensuring they are correctly reflected and propagated.

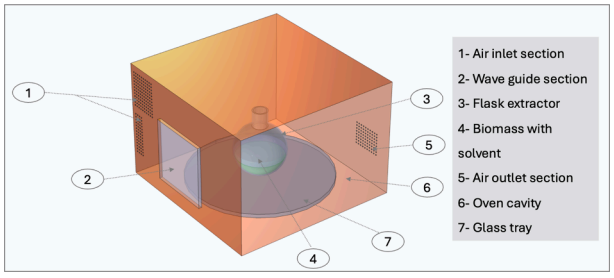

Fig. 1. MW oven geometry containing a glass with extractor flask.

The electromagnetic energy source was integrated using the coaxial port boundary condition [32,34]. Consequently, in this model, the power absorbed per unit volume, Q resulting from the interaction of the microwave with the dielectric sample, is expressed as:

$$Q = \frac{1}{2}\omega\varepsilon_0\epsilon''|E|^2 \tag{9}$$

where |E| is the modulus of the electric field, ω is the angular frequency of the microwaves.

$$\omega = 2\pi f \tag{10}$$

where ϵ_0 is the vacuum permittivity, a physical constant that describes how the electric field behaves in a vacuum.

2.3.3. Fluid dynamics

This module used two physical interfaces: free fluid (air inside the microwave and at the top inside the extractor flask) and fluid in a porous medium (solvent with biomass). The dynamics of the free fluid are described as compressible fluids, while the fluid in the porous medium is described as time-dependent incompressible fluids.

2.3.3.1. Free fluid dynamics in microwave. The airflow velocity inside the microwave is generally low [35]. In this case, an incompressible laminar flow model was developed under steady-state conditions, assuming that the air-fluid in the system quickly reaches a steady state.

$$\boldsymbol{\rho_a}(\boldsymbol{u}\cdot\nabla)\boldsymbol{u} = -\nabla p + \nabla\cdot\left(\left(\mu_a(\nabla\boldsymbol{u} + (\nabla\boldsymbol{u})^\tau) - \frac{2}{3}\mu_a(\nabla\cdot\boldsymbol{u})I\right)\right) + F \tag{11}$$

$$\nabla\cdot(\boldsymbol{\rho u}) = 0 \tag{12}$$

where **u** is the velocity vector (m/s), μ_a is the dynamic fluid viscosity (Pa-s), ρ_a fluid density (kg/m^3), p is the pressure (Pa), I is the identity matrix, superscript T denotes the transpose operator and, F is external volume forces (kg/(m^2·s^2)). For the boundary conditions, the velocity is zero on all walls and surfaces, while the inlet flux velocity is set to 0.1 m/s, as estimated by Arballo et al. [32].

2.3.3.2. Model of solid–liquid extraction. Extractives such as astaxanthin are extracted from biomass using the solid–liquid extraction principle. The model describing this process is based on the transport of species (extractives) in porous media (biomass matrix), mathematically described by Fick's second law.

$$\frac{\partial(\boldsymbol{\theta_L c_i})}{\partial \boldsymbol{t}} + \frac{\partial(\boldsymbol{\rho c_{p,i}})}{\partial \boldsymbol{t}} = \nabla\cdot(\boldsymbol{D_{D,i}} + \boldsymbol{D_{e,i}})\nabla\boldsymbol{c_i} + \boldsymbol{R_i} \tag{13}$$

where ci (mol/m^3) represents the concentration of extractives i in the liquid phase, t(s) denotes time, $c_{P,\,i}$ (mol/(kg of the solid)), $\theta_L(-)$ liquid volume fraction, $D_{D,i}$ (m^2/s) and $D_{e,i}$ (m^2/s) are the dispersion tensor and diffusion coefficient, ρ (kg/m^3) is the density of the liquid, and Ri is an expression for the reaction rate.

The $D_{e,i}$ can be expressed using the following equation, considering the effective tortuosity factor in saturated media:

$$D_{e,i} = {\varepsilon_p}^{4/3} D_{AB,i} \tag{14}$$

The binary diffusivity ($D_{AB,i}$) between extract and solvent can be estimated from the correlation proposed by Wilke and Chang [36].

$$D_{AB,i} = \frac{7.4x10^{-8}T\sqrt{(\varphi M_B)}}{\mu_B {V_A}^{0.6}} \tag{15}$$

where φ, the solvent association parameter, is precisely determined to be

2.26 for this solvent; V_A is the molar volume of the solute at the boiling point under standard conditions (m^3/mol); μ_B (cP) is the viscosity of the solvent (cP); T(K) is the temperature, and M_B (g/mol) is the molar mass of solvent. The dispersion coefficient can be approximated by using the Peclet number (Pe) in porous media:

$$D_{D,i} = \frac{d_p v}{\varepsilon_p Pe} \tag{16}$$

The Peclet number (Pe) can be expressed in terms of the Reynolds number (Re) and the Schmidt number (Sc).

$$Pe = 1.634 Re^{0.265} Sc^{-0.919} \tag{17}$$

$$Sc = \frac{\mu}{\rho D_{AB,i}} \tag{18}$$

The extraction kinetics (Ri) in **Equation (13)** can be defined from the following equation:

$$R_i = \frac{dc_{f,i}}{dt} = k_i \cdot (c_{eq,i} - c_{f,i})^2 \tag{19}$$

where ki (m^3/s·mol) is the reaction rate constant, $c_{f,i}$ (mol/m^3) is the concentration of extract in the fluid phase and $c_{eq,i}$ (mol/m^3) is the concentration of extract at equilibrium conditions.

In the initial conditions: cf,i = 0 at t = 0; and the boundary conditions: cf,i = cf,i at t = t. The following equation is obtained by integrating **Equation (19)**:

$$\frac{1}{(c_{eq,i} - c_{f,i})} - \frac{1}{c_{eq,i}} = k_i t \tag{20}$$

$$c_{f,i} = -\frac{{c_{eq,i}}^2 kt}{1 - c_{eq,i} kt} \tag{21}$$

By rearranging and linearizing the following expression is obtained:

$$\frac{t}{c_{f,i}} = \frac{t}{c_{eq,i}} + \frac{1}{k{c_{eq,i}}^2} = \frac{t}{c_{eq,i}} + \frac{1}{m} \tag{22}$$

$$\frac{t}{c_{f,i}} = \frac{t}{c_{eq,i}} + \frac{1}{m} \tag{23}$$

The coefficient m represents the initial extraction rate when t = 0 equal $k^2_{ceq,i}$. The value of m is estimated from the intercept obtained by plotting $t/c_{f,i}$ versus t using **Equation (23)**.

2.3.4. Heat transfer model

The heat transfer in solid–liquid extraction using MW irradiation can be modeled as heat transfer in a porous medium. The governing equation for this process is given by:

$$(\rho C_p)_{eff} \frac{\partial T}{\partial t} + \rho C_P \boldsymbol{u} . \nabla T + \nabla . q = Q \tag{24}$$

$$q = -k_{eff} \nabla T \tag{25}$$

$$k_{eff} = \varepsilon_p k, \text{ and } (\rho C_p)_{eff} = \varepsilon_p \rho C_p \tag{26}$$

$$(\rho C_p)_{eff} \frac{\partial T}{\partial t} - \nabla . (k_{effs} \nabla T) = Q \text{ for solid} \tag{27}$$

$$k_{effs} = (1 - \varepsilon_p) k_s, \text{ and } (\rho C_p)_{eff} = (1 - \varepsilon_p) \rho_s C_{p,s} \tag{28}$$

where T (K), Cp (J/kg·K), k (W/m·K), and k_s (W/m·K) were temperature, the heat capacity, thermal conductivity of fluid and the thermal conductivity solid, respectively. For this simulation, the heat generated by pressure changes in viscous dissipation has been ignored.

The numerical simulation of ARE extraction by MW was carried out using COMSOL Multiphysics®. The thermal properties and their evolution with air temperature of the microwave glass tray and the extractor flask (also glass) were taken from the COMSOL Multiphysics® database. The physicochemical and thermal properties of the DES ([Ch]Cl:AA) were taken from the literature [37].

The numerical simulation results were compared with experimental data. The accuracy of the model fit was represented by the root mean square error (RMSE); a value was estimated using the following equation:

$$RMSE = \sqrt{\frac{\sum \left(y_{sim}(t) - y_{exp}(t)\right)^2}{N_{point}}} \tag{29}$$

The agreement of the simulated results with the experimental data was evaluated by calculating the coefficient of determination (R^2).

$$R^2 = 1 - \frac{\sum \left(y_{sim}(t) - y_{exp}(t)\right)^2}{\sum \left(y_{sim}(t) - \ddot{y}_{exp}(t)\right)^2} \tag{30}$$

2.3.5. Mesh convergence analysis and computational domain

The mesh used for these simulations contains free tetrahedral elements, with element sizes of predefined normal configurations, except in the biomass zone. Refinement was performed in the extractor flask and porous medium zone (biomass with solvent). Fig. 2 shows the mesh independence study. Different mesh refinement configurations were performed. The variations of normalized ARE concentration extracted with time at 300 W were used for mesh analysis. When the variations do not change with increasing elements, the results are considered

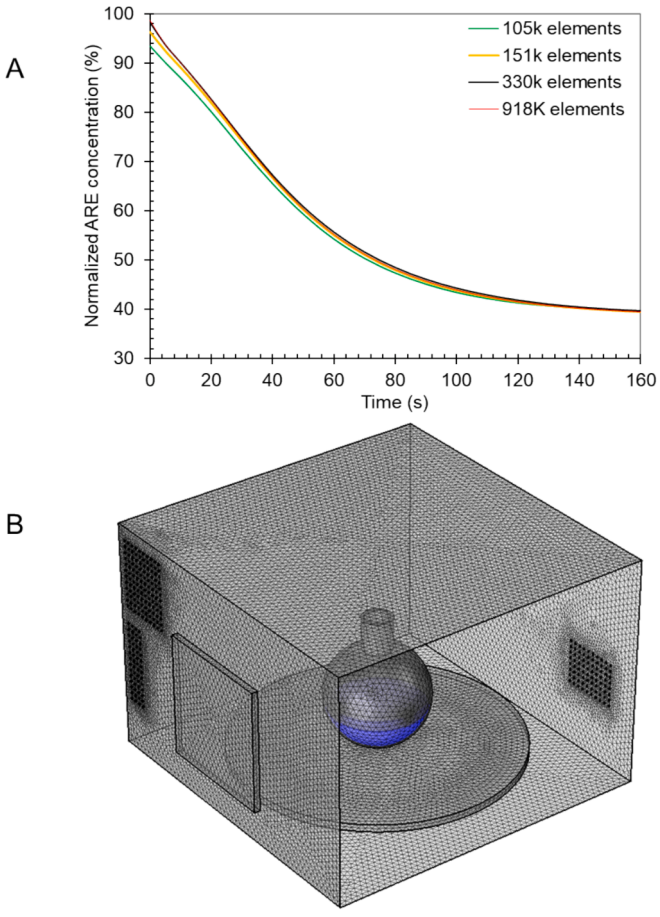

Fig. 2. Mesh independence study: **A-** Effect of number of mesh elements on normalized astaxanthin concentration, **B-** Meshed computational domain.

independent of the number of elements [38]. The mesh-independent results can be used to optimize the extraction condition. Fig. 2**A** shows the results of the variation in the number of mesh elements in normalized ARE concentration.

The average ARE concentration shows negligible variation between 330 k and 918 k elements. Therefore, the simulation requires at least 330 k elements to ensure mesh-independent results. Fig. 2-**B** illustrates the fully meshed 3D geometry used for the subsequent simulation studies.

2.4. Antifungal activity of ARE-rich DES extracts

The antifungal assay was conducted using *Botrytis cinerea* strain 1003, obtained from table grapes berries [39], and *Phytophthora cinnamomi* (*P. cinnamomi*) strain 1858 [40], obtained from walnut orchard soil. Initially, 30 APDA plates were prepared and stored at 6 °C until use. In a laminar flow hood, agar discs were taken from plates with actively growing *B. cinerea* colony and placed on 15 APDA plates. Similarly, agar discs from actively growing *P. cinnamomi* colony, were placed on another 15 APDA plates. After inoculating the microorganisms on the APDA Petri dishes, 50 µl of the respective treatments were added to each plate, applied in a line from one edge to the opposite. After 30 min for the treatments to dry, the plates were sealed with Parafilm and incubated at 22 °C. The treatments for the *B. cinerea* assay included: Control (only *B. cinerea*), *B. cinerea* + [Ch] Cl: AA (1:3), *B. cinerea* + ARE (200 µg/mL solubilized in ethyl acetate and then evaporated), *B. cinerea* + [Ch] Cl: AA (1:3) − ARE (200 µg/mL), and *B. cinerea* + tebuconazole (Tebuconazole 25 % WP, AGROSPEC). For the *P. cinnamomi* assay, the treatments were: Control (only *P. cinnamomi*), *P. cinnamomi* + [Ch]Cl:AA (1:3), *P. cinnamomi* + ARE (200 µg/mL solubilized in ethyl acetate then evaporated), *P. cinnamomi* + [Ch] Cl: AA (1:3) − ARE (200 µg/mL), and *P. cinnamomi* + fosetyl-aluminum (Defense 80 WP, ANASAC). The colony diameters were measured using the cross method after ten days of incubation. Each treatment was replicated three times.

2.5. Colorless residual biomass utilization as biofertilizer

2.5.1. Characterization of residual biomass by SEM-EDS

Samples of bacterial biomass residue were mounted on sample holders and adhered with double-sided carbon tape. Visualization was performed using chemical contrast detectors (Backscatter, BSE) and secondary contrast for topography (UVD) at variable pressure without using any sputtering or critical point dryer, under the following parameters: 15 kV, 50 Pa pressure, WD 10 mm in scanning electron microscope (SEM, Hitachi SU3500, Tokyo, Japan). Images were acquired and analyzed with the Hitachi software driver. An energy-dispersive X-ray spectroscopy (EDS) detector was coupled for quantification and elemental distribution. Three regions of interest (ROI) were selected for each sample to determine the mass percentage and a wider region was used to map the elemental distribution. The acquisition was made under the following parameters: applied energy 20 KV, pressure 50 Pa, WD 10 mm using a scanning electron microscope (Hitachi SU3500, Tokyo, Japan) coupled to XFlash® Detector 410 and Quantax Esprit 1.8.1 software controller (Bruker, Germany).

2.5.2. Experimental design, soil, and plant material

The *in vivo* experiment was carried out during 50 days under greenhouse conditions (25)/21 °C; 50/60 % relative humidity, 14/10 h day/night photoperiod) at the greenhouse of the Universidad de La Frontera, Temuco, Chile. A clay-loam Andisol was collected from Mahuidache (Araucanía Region, Chile) at a 0–20 cm depth. The soil had a pH of 5.8 (measured in water, 2:5 w/v), 15 % organic matter, and nutrient concentrations of (in mg/kg): N, 26; available P, 19; exchangeable K, 211. *Lactuca sativa* seeds of cv. 'Grand Rapids' (GR) were sown on polystyrene trays with a mix of sterilized peat moss/perlite (70:30, v/v). After thirty days the plants were transferred to pots filled with 1,200 g of the soil described above. Two treatments were used in a fully randomized statistical design, plant with and without the addition of 3 g of residual biomass (n = 10). The plants were watered with 100 ml of tap water every other day to keep the soil moisture near field capacity.

2.5.3. Lactuca sativa biomass production, N and P concentrations and photosynthetic traits

The Targas-1 equipment (PP Systems, Amesbury, MA, USA) was used to determine photosynthetic traits, including the leaf internal concentration of CO_2 (Ci: µmol mol^{-1}), photosynthesis rate (A: µmol CO_2 m^{-2} s^{-1}), and stomatal conductance (gs: mmol H_2O m^{-2} s^{-1}), following the instructions provided in the user manual. Measurements were conducted on the second youngest leaf from four plants per treatment, one day before harvest. Fifty days after sowing, the *L. sativa* plants were harvested and weighed to measure their fresh weight. Then, the plant material was dried (65 °C, 48 h) in a forced-air oven, and 0.3 g of tissue was ground and placed in a 100 mL Erlenmeyer flask with 3.3 mL of digest solution (80 % v/v H_2SO_4, 5 % w/v salicylic acid), and incubated overnight at room temperature. The digestion mixture was incubated for 1 h at 180 °C, after which 5 drops of 30 % H_2O_2 were added, and the incubation temperature was raised to 280 °C. Hydrogen peroxide was added until a transparent solution was obtained. Afterward, the digest was cooled and resuspended in 50 mL of ultrapure H_2O. The digestates were used for determination of nitrogen (N) and phosphorus (P). The N content was measured as described by Baethgen & Alley [41] and adapted to an automatic injector Synergy H1 Hybrid Multi-Mode microplate spectrophotometer (BioTek Inc., Winooski, VT, USA). Briefly, 16 µL of digestion mixture and 88 µL of tartrate buffer (0.1 M Na_2HPO_4, 5 % Na-K tartrate, and 5.4 % NaOH) were placed in wells of microplates. Then, 64 µL of salicylate-Na nitroprusside solution (15 % sodium salicylate and 0.03 % sodium nitroprusside) and 32 µL of freshly prepared sodium hypochlorite solution (0.32 % v/v) were added using an automatic injector. The samples were shaken and incubated for 15 min at 37 °C, and absorbance was read at 650 nm. A standard curve of $(NH_4)_2SO_4$ was used to determine the N content in the samples. The P quantification was performed using the colorimetric method following the formation of blue molybdate [42].

2.5.4. Statistical analysis

An analysis of mean comparisons by using the Student́s T-test was performed to evidence significant differences between the control plants and *L. sativa* plants with the addition of bacterial residual biomass. Significance in the means of the data was established at $p < 0.05$. Statistical analyses were carried out using R version 4.3.2.

3. Results and discussion

3.1. Understanding the ARE recovery using MW-assisted extraction

3.1.1. Fluid dynamics inside the MW oven

Inside a MW, airflow can be influenced by natural convection and forced convection, each contributing differently to the overall flow pattern within the cavity and extractor flask during the extraction. Natural convection occurs inside the extractor flask and is driven by temperature gradient. As shown in Fig. 3-**A,** the hot airflow rises from the surface of the samples (composed of DES and *P. carotinifaciens* biomass) towards the top of the extractor, where the outlet is located. This movement creates a cycle in which the hot airflow rises and moves toward the cooler zones. The maximum flow velocity in this process is relatively low, around 0.002 m/s at 120 s of extraction. This airflow generated by heating the DES is not strong enough to significantly affect the heat distribution in the MW cavity.

On the other hand, forced convection occurs inside the MW cavity and is characterized by the movement of fresh airflow from an inlet to an outlet at a velocity of about 0.1 m/s, as shown in Fig. 3-**B**. The airflow

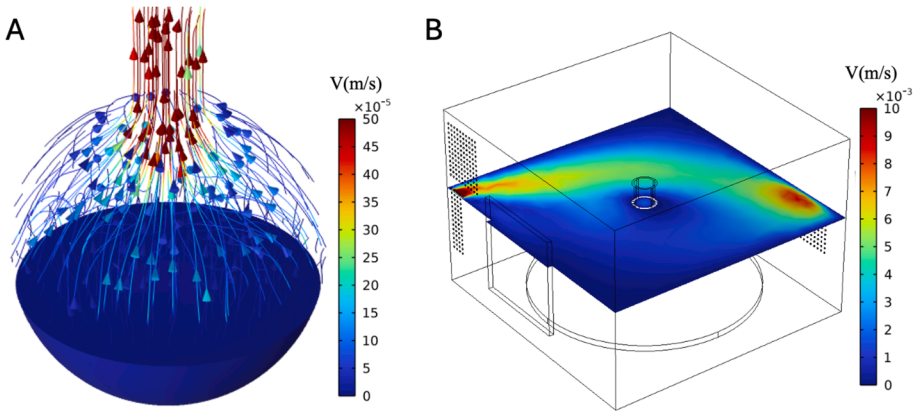

Fig. 3. Fluid dynamics inside the MW: **A-** streamlines and velocity vectors (arrows) in the extractor flask, **B-** velocity magnitude profile at the height medium of the cavity.

inside a MW oven, highlighting the zones where the air velocities reach their maximum values, specifically at the inlet and outlet of the oven cavity. These simulations were performed considering the presence of an extraction flask inside the oven, which influences the airflow pattern. The arrangement of the flask affects how the air moves inside the cavity, particularly when entering at maximum velocity and when exiting, adjusting to the geometry and contents of the oven. This forced flow is distinct from the upward flow caused by natural convection. In this case, there is no interaction between natural and forced convection within the MW.

3.1.2. *Electromagnetic field distribution*

Fig. 4 shows the distribution of the electric field or electromagnetic waves (EMW) in the z-direction inside a MW oven based on the results analysis of the simulation of Maxwell's equations. The distribution is non-uniform, with peaks and valleys indicating the maximum and minimum of the electric field. The maximum value of the electric field inside the oven was 3.05 × 104 V/m, found near the center at the bottom. Similar results were reported by Arballo et al. [32].

High electric field strength near the base, especially around the turntable, is a domestic MW oven design feature. This configuration ensures that the area where the sample will be heated receives the maximum possible energy, increasing heat absorption efficiency. The turntable's rotation helps distribute the energy evenly across the sample, reducing the risk of uneven heating. However, despite the configuration and design, the inherent non-uniformity of the electric field distribution can lead to the formation of "hot points" and "cold points." These variations are caused by the fluctuating electric field strength, which affects how much MW energy is absorbed in different areas. In applications where uniform heating is important, such as extraction processes, these fluctuations can be problematic, leading to non-uniform extraction of molecules of interest. As was implemented in this study's experiment, a stirring system can be employed to reduce the problem of temperature non-uniformity. This system allows a relatively uniform temperature to be achieved inside the extractor flask. In this simulation, stirring was not considered to reduce the computational time.

From a design point of view, CFD simulation provides insight into electric field distribution patterns. This is essential for improving the

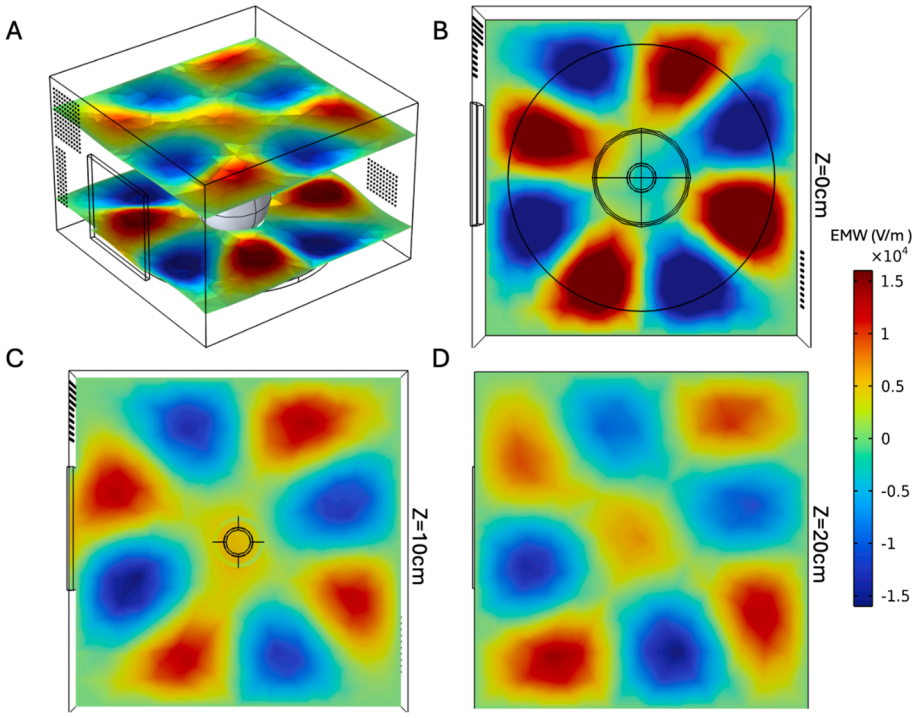

Fig. 4. Electromagnetic field distribution inside the MW oven: **A-** z-component of the electric field, (**B-D**) electric field slices at different heights (z) inside the MW.

performance of MW ovens. The knowledge gained can also be used to refine the cavity geometry, adjust the location and power of the MW sources, and optimize the rotational speed of the turntable. These improvements aimed to smooth the electric field distribution, thus promoting more uniform heating and increasing overall efficiency.

3.1.3. MW oven heating and temperature distribution

The interaction and absorption of MW radiation influence the temperature distribution inside a MW during heating. The heating of the DES in a MW is due to the interaction between the waves and the DES components. The waves generate an alternating electric field that mainly affects the molecules, causing them to rotate and generating heat through friction. This electric field interacts with the molecules of the dielectric material, generating heat through a process known as dielectric heating. This phenomenon increases the temperature of the samples inside the MW. The simulation results of the evolution of the average temperature inside the pure solvent were compared with experimental data determined at a point inside the extractor flask, as shown in Fig. 5-**A**. The simulation results accurately predict the solvent temperature increase at different powers, 300, 360, and 420 W. The RMSE values between experimental and simulated were 27.98, 33.79 and 25.22 °C, corresponding to R^2 of 0.813, 0.870 and 0.934 for powers of 300, 260 and 420 W, respectively. The differences between the simulation results and the experimental data can be attributed to the fact that the experimental data were obtained at a specific point in the stirred bioreactor system, while the simulated results correspond to the average temperatures inside the reactor fluid.

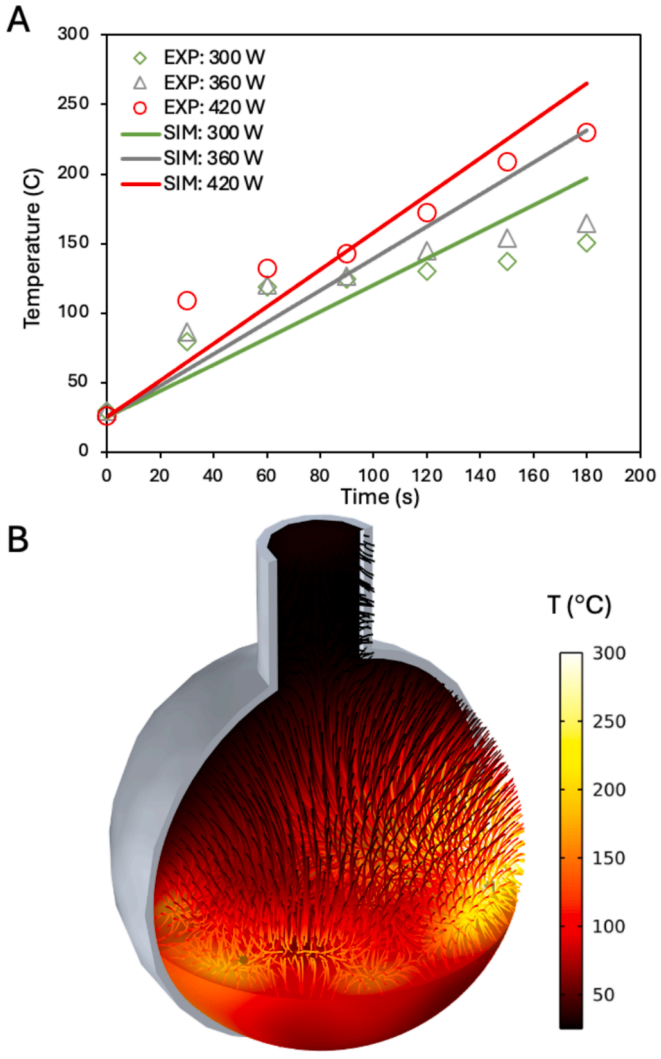

Fig. 5. MW oven heating: **A-** experimental and simulated temperature evolution in the solvent at 300, 360 and 420 W, **B-** temperature distribution inside the extractor flask (biomass and DES).

In a MW oven, the temperature distribution inside the cavity and in the samples (biomass and solvent) is not uniform due to the propagation modes of electromagnetic waves, as explained above (**section 3.1.2**).

In MW, interference and resonance patterns generate "hot points" and "cold points". Moreover, variations in the absorption capabilities of materials, determined by their dielectric properties, result in a non-uniform temperature distribution. This stands in contrast to dimensionless models, which assume spatial uniformity and oversimplify the complexities of experimental conditions. Fig. 5-**B** shows the spatial temperature variations after a heating time of 120 s at 300 W (condition selected to avoid the degradation of ARE from bacterial biomass). The samples different "hot points" are identified. These spatial variations of temperature are important to understand the heating process in the MW oven.

3.1.4. Extraction kinetics of ARE and numerical model validation

The pseudo-second-order model was used to analyze the kinetics of ARE extraction using the MW. Initially, the ARE concentration at equilibrium was determined from the experimental data. Following this, kinetic parameters were estimated by minimizing the RMSE as the objective function, including the apparent activation energy and pre-exponential factor.

The accuracy of the model predictions relative to the experimental data was evaluated using RMSE and the R^2. The ARE concentration reaches equilibrium in the reactor at 51.47 mol/m^3, corresponding to an ARE yield of 12.29 mg/g. The kinetic parameters, including an activation energy of 52 kJ/mol and a pre-exponential factor of 1.2×10^4 s^{-1}, were fitted to the experimental data, resulting in an RMSE = 1.46 and an R^2 = 0.974. Fig. 6 compares the simulation results and experimental data for ARE extraction. The kinetic parameters used in the simulation accurately predicted the extraction rate up to the point of equilibrium, as shown in Fig. 6-**A**.

To further validate these predictions, the results obtained by CFD simulations were compared with experimental data collected at different extraction times (0, 30, 60, 90, and 120 s) under a power of 300 W (optimal conditions to avoid the degradation of ARE). Fig. 6-**B** illustrates this comparison, highlighting how closely the CFD simulation results matched the experimental observations. This comparison is essential to confirm the model's accuracy and ability to replicate the exact behavior of the extraction process, which is fundamental to optimizing the MW-based extraction process.

In general, this section focuses on understanding the behavior of this non-conventional method for extracting ARE from *P. carotinifaciens* biomass using MW assisted extraction with a neoteric solvent such as DES composed of ChCl and AA (1:3) The MW system was meticulously modeled to optimize parameters such as microwave power, temperature distribution, and fluid dynamics within the microwave oven using a CFD modeling to analyze the fluid dynamics and electromagnetic field distribution, providing a comprehensive understanding of the ARE extraction process using DES. This comprehensive approach ensures uniform heating and effective ARE-DES interactions, critical for maximizing astaxanthin yield. By employing a bio-based DES, the study aims to enhance both the extraction efficiency and the sustainability of the process. However, when discussing biorefinery sustainability, the complete valorization of biomass and solvent recycling is crucial to reducing costs and environmental impact. After the extraction of ARE from *P. carotinifaciens* biomass using MW, the mixture is centrifuged to separate the ARE-rich DES extracts from the residual colorless biomass. DES, particularly those composed of choline chloride, are very difficult to recover and recycle due to their strong interactions, low vapor pressure and stability, posing a significant challenge in maintaining the overall sustainability of the process. This problem makes it difficult and

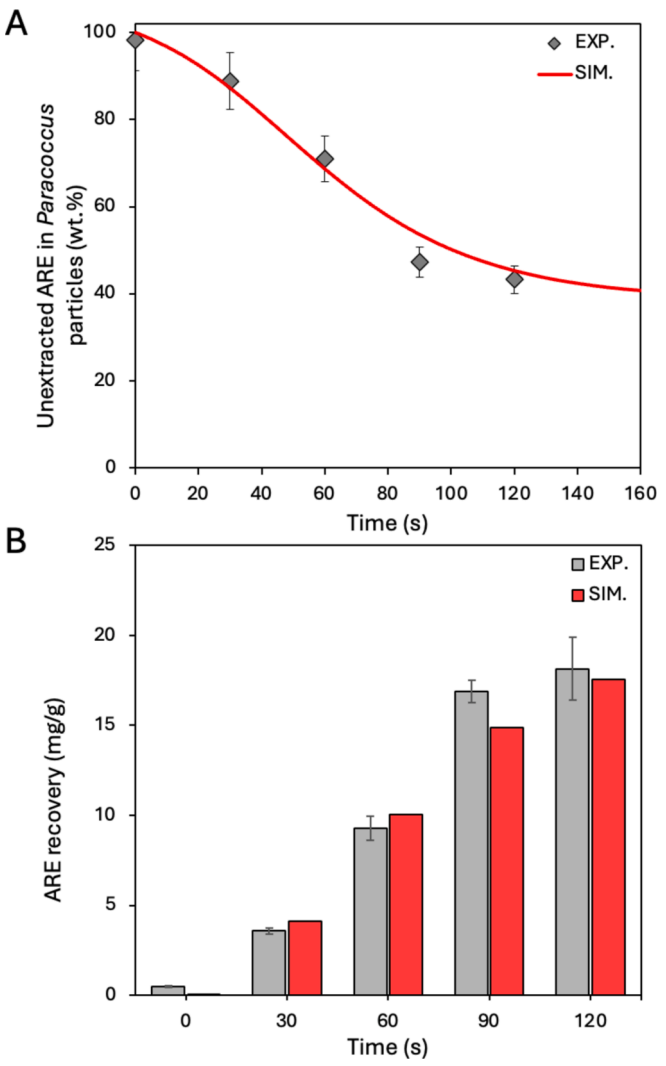

Fig. 6. Evolution of experimental data and simulated results at 300 W: **A-** unextracted ARE in *P. carotinifaciens* biomass, **B-** astaxanthin-rich extract recovery.

costly to recover pure ARE from these solvents. To overcome these drawbacks, the next phase of this research focused on the direct application of ARE-rich DES extracts as antifungal agents against pathogens such as *B. cinerea* and *P. cinnamomi,* which affect crops like grapes, strawberries, and avocados envisioning its application as antifungal agents in agriculture. Meanwhile, the colorless residual *P. carotinifaciens* biomass that remained from the centrifuge unit was characterized and employed as a sustainable biofertilizer, demonstrating the potential for full utilization of the *P. carotinifaciens* biomass and contributing to the circular economy in agricultural applications.

3.2. ARE-rich DES extracts effect against pathogens

This study assessed the potential of ARE-rich DES extracts as antifungal agents. Initially, intracellular ARE was extracted from *P. carotinifaciens* biomass using bio-based DES. Rather than opting for purification, we utilize the extracts directly due to their inherent richness in ARE and DES with established antifungal properties. Directly assessing these extracts simplified the process, cutting out additional purification steps and reducing bioprocessing costs. The antifungal efficacy of these ARE-rich DES extracts was tested against *B. cinerea* and *P. cinnamomi.* These pathogens were selected for their significance as plant pathogens, causing substantial economic losses in agriculture *viz.*, *B. cinerea*, commonly known as gray mold, is notorious for affecting a broad spectrum of crops, including table grapes [39], strawberries [43], and tomatoes, leading to fruit rot and spoilage. On the other hand, *P. cinnamomi* is a soilborne pathogen responsible for root rot in various plants, notably avocado [44] and walnut trees [40]. Assessing the antifungal activity of the ARE-rich DES extracts against these specific pathogens is crucial for determining their effectiveness and potential application in agricultural disease management (Fig. 7). This approach offers an environmentally friendly alternative to conventional chemical fungicides, contributing to sustainable agricultural practices.

Based on the results shown in Fig. 7**-B**, the *in vitro* inhibition percentages indicate that the treatments [Ch]Cl:AA (1:3), ARE, and [Ch]Cl:AA (1:3) – ARE (200 μg/mL) significantly inhibit the growth of the pathogen *P. cinnamomi* (strain 1858), with inhibition rates of 51.85 %, 43.39 %, and 56.61 %, respectively, compared to the control. A synergistic effect is observed in the treatment combining [Ch]Cl:AA (1:3) and ARE, as it is the only treatment that significantly outperforms the fosetyl-aluminum (commercial antifungal) treatment. The fosetyl-aluminum treatment has two modes of action: in vitro inhibition and stimulation of plant defense mechanisms (Coffey), thus enhancing its efficacy *in vivo*. Similarly, as shown in Fig. 7**-C**, the treatments [Ch]Cl:AA (1:3) and [Ch]Cl:AA (1:3) – ARE (200 μg/mL) exhibit significant control over the mycelium growth of *B. cinerea* (strain 1003) compared to the control treatment. The [Ch]Cl:AA (1:3) treatment achieved 48.37 % inhibition, while the [Ch]Cl:AA (1:3) – ARE treatment achieved 51.09 % inhibition relative to the control. The [Ch]Cl:AA (1:3) – ARE treatment demonstrates a synergistic effect, significantly outperforming the ARE-only treatment, unlike the [Ch]Cl:AA (1:3) treatment. Previous studies have shown that ARE exhibits effective antifungal activity against both *C. albicans* and *C. glabrata*. Standard AXT reduced 90 % (MIC90) of *C. albicans* and *C. glabrata* growth within the concentration range of 500–800 μg/mL, while isolated AXT inhibited growth within the range of 500–800 μg/mL and 800–1000 μg/mL. For *C.albicans*, the MFC value of AXT (800 μg/mL) was the same as the standard, whereas for *C. glabrata*, it reached up to 1000 μg/mL. Exposure to sub-inhibitory concentrations (500 μg/mL) of AXT induced changes in the morphology of both biofilm cells [45]. In another work, [Ch]Cl-based DES revealed antifungal activities against *B. cinerea, C. acutatum, A. radicina and F. graminearum* at 10 and 100 μg/mL [46].

Exploring the antifungal properties of ARE-rich DES extracts directly, without purification on the growth of *Botrytis* and *Phytophthora in vitro* yielded promising results that proved advantageous due to their inherent richness in ARE and DES, simplifying the process and reducing costs. Notably, treatments combining [Ch]Cl:AA (1:3) with ARE demonstrated significant inhibition of some pathogens growth, highlighting the potential of ARE-rich DES extracts as eco-friendly alternatives to conventional synthetic and harmful fungicides in agricultural disease management.

3.3. Residual bacterial biomass application as biofertilizer for plant growth (Lactuca sativa)

3.3.1. Characterization of the residual biomass

The residual bacterial biomass exhibited a fine granulometry, with particles typically smaller than 50 μm (Fig. 8**-A**). The residue's composition is predominantly organic, with a high proportion of C and O; however, a significant proportion of Ca stands out in its structure (Fig. 8**-B**). This element was observed to have a high presence in all samples analyzed by SEM and EDX (Fig. 8**-B**). The notable presence of Ca in the sample is due to the use of $CaCO_3$ as an excipient in the stabilization process of bacterial biomass during the preservation process, resulting in its residual presence due to low solubility. In moderately acidic soils, the application of compounds such as $CaCO_3$ is beneficial [47], as it produces an alkalizing effect in the rhizosphere, making other nutrients like N, P, and K more available to plants, thus promoting their growth and nutritional status [48,49].

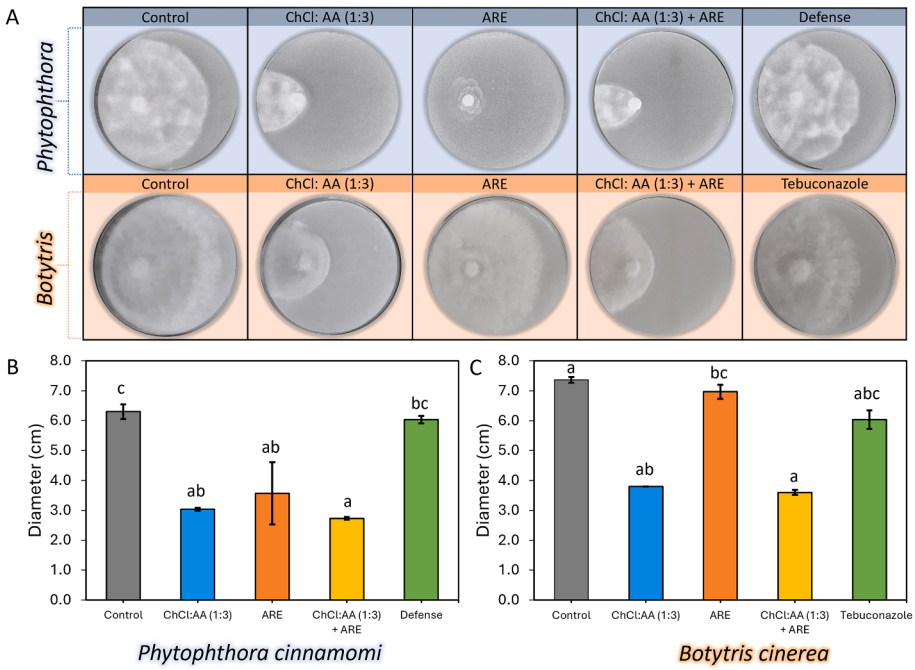

Fig. 7. A- Mycelial morphology of *B. cinerea* and *P. cinnamomi* treated with ARE, ARE-DES extracts, and commercial fungicides. **B-** Colony growth diameter for *P. cinnamomi* mycelium treated with the control (only *P. cinnamomi*), *P. cinnamomi* + [Ch]Cl:AA (1:3), *P. cinnamomi* + ARE (200 μg/mL), *P. cinnamomi* + [Ch]Cl:AA (1:3) − ARE (200 μg/mL), and *P. cinnamomi* + fosetyl-aluminum (Defense 80 WP, ANASAC). **C-** Colony growth diameter for in vitro control of *B. cinerea* treated with the control (only *B. cinerea*), *B. cinerea* + [Ch]Cl:AA (1:3), *B. cinerea* + ARE (200 μg/mL), *B. cinerea* + [Ch]Cl:AA (1:3) − ARE (200 μg/mL), and *B. cinerea* + tebuconazole (Tebuconazole 25 % WP, AGROSPEC).

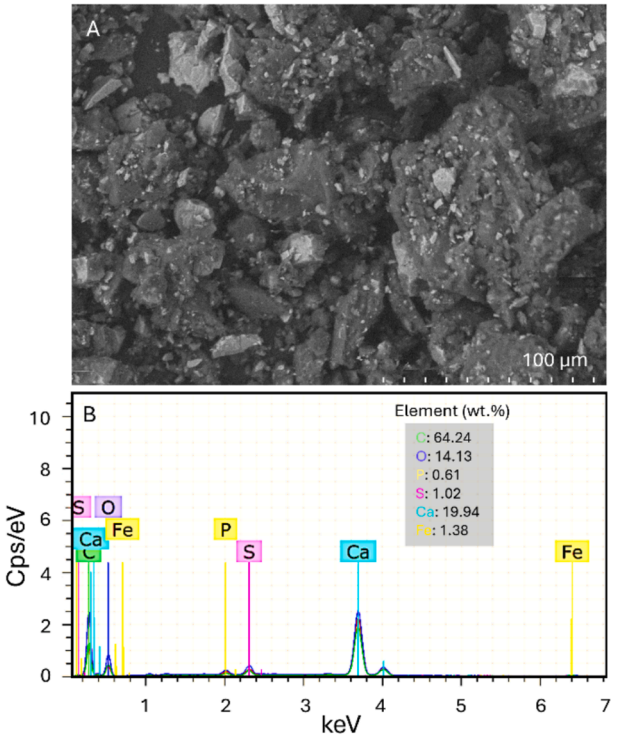

Fig. 8. A- Scanning Electron Microscopy (SEM) of *Paracoccus carotinifaciens* biomass residue after ARE extraction procedure. **B-** Energy-Dispersive X-ray (EDX) analysis of the residue showing the main elements and elemental composition in mass percent of the main elements present in the bacterial biomass residue (note the high proportion of Ca).

3.3.2. *Effects of the residual biomass as biofertilizer in Lactuca sativa plants*

As shown in Fig. 9- **A,B**, the beneficial effect on the growth of *L. sativa* plants is visually evident, with larger plants obtained when bacterial residual biomass was added to the soil. In detail, plants treated with the residue produced 69 % more biomass than those without the addition of bacterial residue (Fig. 9-**C**). Moreover, although the concentrations of the main nutrients analyzed (N and P) did not differ between the treatments, the uptake from the soil was significantly higher in plants grown with the residue addition (Fig. 9-**D-G**). Despite the low N and P contents in the bacterial residue, the increase in their uptake can be attributed to two main factors*: i)* the high content of presumably labile organic C sources, which may have facilitated the proliferation of heterotrophic organisms in the rhizosphere, thereby activating nutrient cycling properties, especially N fixation and phosphate solubilization [50]; and *ii)* the increase in rhizosphere pH, which among other effects enhances nutrient availability concomitantly reducing soluble concentrations of Al^{3+}, particularly affecting P availability in volcanic soils as the here used [49]. Finally, although only A among the determined physiological characteristics showed significant differences in favor of plants with bacterial colorless residue addition, applying the residue increased the trend (Fig. 9-**H-K**). Our results demonstrate the biofertilizer potential of the studied bacterial residue, especially in moderately acidic soils, and highlight its value in enhancing food production. The mechanistic aspects of this increase in production, nutrient absorption, and plant physiological improvement need further investigation in our near studies.

4. Conclusions

This study demonstrates the feasibility and potential of a zero-waste bacterial-based biorefinery for extracting astaxanthin-rich extracts (ARE) using microwave (MW)-assisted deep eutectic solvents (DES) from *Paracoccus carotinifaciens*. The CFD simulations confirmed that natural and forced convection play distinct roles in airflow patterns, while the non-uniform electric field distribution highlighted areas for

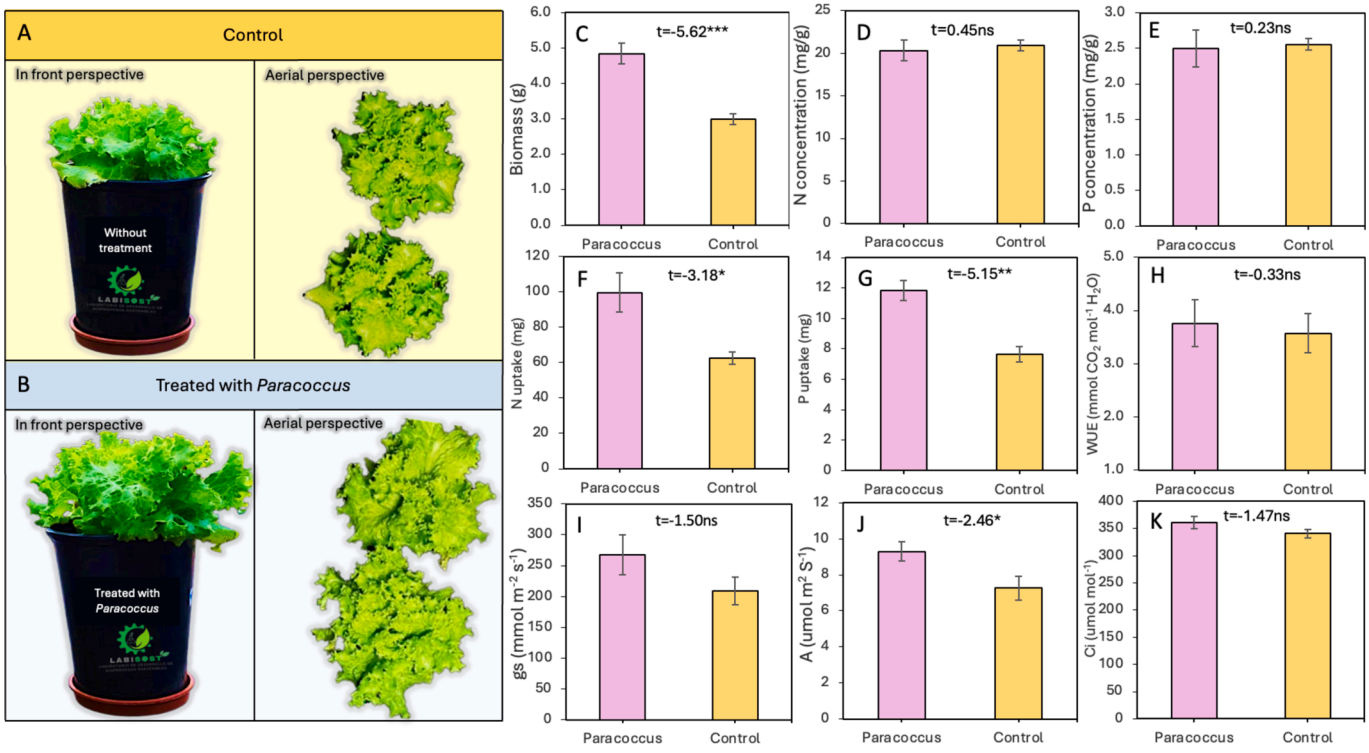

Fig. 9. **A-** Visual perspective of a representative experimental individual of *Lactuca sativa* plants without addition of bacterial biomass residue. **B-** Visual perspective of a representative experimental individual of *L. sativa* plants with the addition of *Paracoccus carotinifaciens* biomass residue. **C-** *L. sativa* plants dry weight. **D-** *L. sativa* plants N concentration. **E-** *L. sativa* plants P concentration. **F-** *L. sativa* plants total N uptake. **G-** *L. sativa* plants total P uptake. **H-** *L. sativa* plants water use efficiency. **I-** *L. sativa* plants stomatal conductance. **J-** *L. sativa* plants net CO_2 assimilation rate. **K-** *L. sativa* plants CO_2 internal concentration.

potential design improvements to enhance heating uniformity. The recovery of ARE using the optimized MW-assisted DES extraction method reached equilibrium at 51.47 mol/m3, corresponding to a yield of 12.29 mg/g. The CFD simulations provided accurate predictions of the extraction kinetics, with an RMSE of 1.46 and R2 of 0.974, validating the model's effectiveness in replicating the experimental extraction process. The effectiveness of ARE-rich DES extracts as antifungal agents was validated, showing significant inhibition rates. Specifically, treatments combining [Ch]Cl (1:3) with ARE achieved inhibition rates of 56.61 % against *P. cinnamomi* and 51.09 % against *B. cinerea*, indicating their potential as eco-friendly alternatives to conventional fungicides in agriculture. Moreover, the residual colorless biomass of *P. carotinifaciens* post-extraction was characterized and utilized as a biofertilizer, demonstrating a beneficial impact on *Lactuca sativa* (lettuce) growth. The residual biomass significantly increased plant biomass by 69 % and enhanced nutrient uptake, likely due to its composition and the resulting enhancement of soil properties. This work underscores the integration of ARE-rich DES extracts in agriculture and the application of residual biomass as a biofertilizer contribute to the circular economy, highlighting the potential of this biorefinery model to advance both economic and environmental sustainability in bio-based industries.

CRediT authorship contribution statement

Cassamo U. Mussagy: Conceptualization, Investigation, Data curation, Writing – original draft, Writing – review & editing, Visualization, Funding acquisition, Supervision. **Angie V. Caicedo Paz:** Investigation, Writing – review & editing. **Pablo Cornejo:** Investigation, Writing – review & editing. **Christian Santander:** Investigation. **Felipe González:** Investigation. **Rafael G. Voloua:** . **Ximena Besoain:** Investigation, Formal analysis. **Alejandra Larach:** Investigation. **Aldo Salinas:** Investigation. **Karina Godoy:** Investigation. **Diakaridia Sangaré:** Conceptualization, Investigation, Formal analysis, Data curation, Writing – original draft, Writing – review & editing, Visualization.

Funding

This research was supported by grants 039.300/2024 from VINCI-DI (PUCV), ANID/FORTALECIMIENTO CENTROS REGIONALES/CERES/R23F0003, ANID/FONDAP/15130015, ANID/FONDAP/1523A0001and ANID/FONDECYT/1210964.

Declaration of competing interest

The authors declare that they have no known competing financial interests or personal relationships that could have appeared to influence the work reported in this paper.

Data availability

Data will be made available on request.

References

[1] C.U. Mussagy, D. Remonatto, F.P. Picheli, A.V. Paula, R.D. Herculano, V.C. Santos-Ebinuma, R.L. Farias, B.S.D. Onishi, S.J.L. Ribeiro, J.F.B. Pereira, A. Pessoa Jr, A look into Phaffia rhodozyma biorefinery: From the recovery and fractionation of carotenoids, lipids and proteins to the sustainable manufacturing of biologically active bioplastics, Bioresour. Technol. 362 (2022) 127785, https://doi.org/10.1016/j.biortech.2022.127785.

[2] G. Baskar, R. Aiswarya, G. Kalavathy, A. Pandey, E. Gnansounou, J.K. Raman, R. Praveen Kumar, A Biorefinery approach towards development of renewable platform chemicals from sustainable biomass, in: Refining Biomass Residues for Sustainable Energy and Bioproducts, Elsevier, 2020: pp. 135–147. DOI: 10.1016/B978-0-12-818996-2.00006-5.

[3] J. Monte, C. Ribeiro, C. Parreira, L. Costa, L. Brive, S. Casal, C. Brazinha, J. G. Crespo, Biorefinery of dunaliella salina: sustainable recovery of carotenoids, polar lipids and glycerol, Bioresour. Technol. (2020), https://doi.org/10.1016/j.biortech.2019.122509.

[4] P.A. Aneesh, R. Anandan, L.R.G. Kumar, K.K. Ajeeshkumar, K.A. Kumar, S. Mathew, A step to shell biorefinery—Extraction of astaxanthin-rich oil, protein, chitin, and chitosan from shrimp processing waste, Biomass Convers Biorefin (2020), https://doi.org/10.1007/s13399-020-01074-5.

[5] S. Venkata Mohan, G.N. Nikhil, P. Chiranjeevi, C. Nagendranatha Reddy, M.V. Rohit, A.N. Kumar, O. Sarkar, Waste biorefinery models towards sustainable circular bioeconomy: Critical review and future perspectives, Bioresour Technol 215 (2016) 2–12. DOI: 10.1016/j.biortech.2016.03.130.

[6] R. Torres de Oliveira, M. Ghobakhloo, S. Figueira, Industry 4.0 towards social and environmental sustainability in multinationals: Enabling circular economy, organizational social practices, and corporate purpose, J. Clean Prod. 430 (2023) 139712, https://doi.org/10.1016/j.jclepro.2023.139712.

[7] P.K. Mukherjee, B. Das, P.K. Bhardwaj, S. Tampha, H.K. Singh, L.D. Chanu, N. Sharma, S.I. Devi, Socio-economic sustainability with circular economy — An alternative approach, Sci. Total Environ. 904 (2023) 166630, https://doi.org/10.1016/j.scitotenv.2023.166630.

[8] P.K. Singh, P. Shukla, S.K. Verma, S. Mishra, P.K. Parhi, Zero-Waste Biorefineries for Circular Economy, in: Biotechnology for Zero Waste, Wiley, 2022: pp. 439–456. DOI: 10.1002/9783527832064.ch29.

[9] C.U. Mussagy, Advances in microbial astaxanthin production, In (2024), https://doi.org/10.1016/bs.aambs.2024.05.001.

[10] H. Inoue, S. Shimamoto, H. Takahashi, Y. Kawashima, S. Wataru, D. Ijiri, A. Ohtsuka, Effects of astaxanthin-rich dried cell powder from *Paracoccus carotinifaciens* on carotenoid composition and lipid peroxidation in skeletal muscle of broiler chickens under thermo-neutral or realistic high temperature conditions, Anim. Sci. J. 90 (2019) 229–236, https://doi.org/10.1111/asj.13141.

[11] M. Sztretye, B. Dienes, M. Gönczi, T. Czirják, L. Csernoch, L. Dux, P. Szentesi, A. Keller-Pintér, Astaxanthin: a potential mitochondrial-targeted antioxidant treatment in diseases and with aging, Oxid. Med. Cell Longev. 2019 (2019) 1–14, https://doi.org/10.1155/2019/3849692.

[12] C.U. Mussagy, L. Dufossé, A review of natural astaxanthin production in a circular bioeconomy context using Paracoccus carotinifaciens, Bioresour. Technol. 369 (2023) 128499, https://doi.org/10.1016/J.BIORTECH.2022.128499.

[13] C.U. Mussagy, N.F. Ramos, A. V. Caicedo P., F.O. Farias, M. Ahmad, A. Mustafa, V. Raghavan, Tuning bio-derived solvents for the rapid solubilization of astaxanthin-rich extracts from non-conventional bacterium Paracoccus carotinifaciens, Sep. Purif. Technol. 346 (2024) 127542. DOI: 10.1016/j.seppur.2024.127542.

[14] K.S. Khoo, S.Y. Lee, C.W. Ooi, X. Fu, X. Miao, T.C. Ling, P.L. Show, Recent advances in biorefinery of astaxanthin from Haematococcus pluvialis, Bioresour. Technol. 288 (2019) 121606, https://doi.org/10.1016/j.biortech.2019.121606.

[15] X. Li, X. Wang, C. Duan, S. Yi, Z. Gao, C. Xiao, S.N. Agathos, G. Wang, J. Li, Biotechnological production of astaxanthin from the microalga Haematococcus pluvialis, Biotechnol. Adv. 43 (2020) 107602, https://doi.org/10.1016/j.biotechadv.2020.107602.

[16] A. Vanessa Caicedo Paz, F. Rigano, C. Cafarella, A. Tropea, L. Mondello, J. Paul Martinez Galan, M. Ahmad, A. Mustafa, F. Farias, A. Córdova, D. Giuffrida, L. Dufossé, C. Ussemane Mussagy, Process intensification of ultrasound assisted deep eutectic solvent-based extraction of astaxanthin-rich extract derived from the non-conventional bacterium Paracoccus carotinifaciens, Sep. Purif. Technol. 339 (2024) 126674. DOI: 10.1016/j.seppur.2024.126674.

[17] B. Kim, S. Youn Lee, A. Lakshmi Narasimhan, S. Kim, Y.K. Oh, Cell disruption and astaxanthin extraction from Haematococcus pluvialis: Recent advances, Bioresour. Technol. 343 (2022) 126124. DOI: 10.1016/J.BIORTECH.2021.126124.

[18] X. Zhou, W. Ding, W. Jin, Microwave-assisted extraction of lipids, carotenoids, and other compounds from marine resources, Innovative and Emerging Technologies in the Bio-Marine Food Sector: Applications, Regulations, and Prospects (2022) 375–394. DOI: 10.1016/B978-0-12-820096-4.00012-2.

[19] L. Zhao, G. Chen, G. Zhao, X. Hu, Optimization of microwave-assisted extraction of astaxanthin from haematococcus pluvialis by response surface methodology and antioxidant activities of the extracts, Sep Sci Technol 44 (2009) 243–262, https://doi.org/10.1080/01496390802282321.

[20] A.N. Nunes, A. Roda, L.F. Gouveia, N. Fernández, M.R. Bronze, A.A. Matias, Astaxanthin extraction from marine crustacean waste streams: an integrate approach between microwaves and supercritical fluids, ACS Sustain. Chem. Eng. 9 (2021) 3050–3059, https://doi.org/10.1021/ACSSUSCHEMENG.0C06534/SUPPL_FILE/SC0C06534_SI_001.PDF.

[21] F.P. Byrne, S. Jin, G. Paggiola, T.H.M. Petchey, J.H. Clark, T.J. Farmer, A.J. Hunt, C. Robert McElroy, J. Sherwood, Tools and techniques for solvent selection: green solvent selection guides, Sustain. Chem. Processes 4 (2016) 7, https://doi.org/10.1186/s40508-016-0051-z.

[22] D. Prat, A. Wells, J. Hayler, H. Sneddon, C.R. McElroy, S. Abou-Shehada, P.J. Dunn, CHEM21 selection guide of classical- and less classical-solvents, Green Chem. 18 (2016) 288–296, https://doi.org/10.1039/C5GC01008J.

[23] F.P. Byrne, S. Jin, G. Paggiola, T.H.M. Petchey, J.H. Clark, T.J. Farmer, A.J. Hunt, C.R. Mcelroy, J. Sherwood, Tools and techniques for solvent selection: green solvent selection guides, Sustain Chem Process 4 (2016) 7, https://doi.org/10.1186/s40508-016-0051-z.

[24] B.B. Hansen, S. Spittle, B. Chen, D. Poe, Y. Zhang, J.M. Klein, A. Horton, L. Adhikari, T. Zelovich, B.W. Doherty, B. Gurkan, E.J. Maginn, A. Ragauskas, M. Dadmun, T.A. Zawodzinski, G.A. Baker, M.E. Tuckerman, R.F. Savinell, J. R. Sangoro, Deep eutectic solvents: a review of fundamentals and applications, Chem. Rev. 121 (2021) 1232–1285, https://doi.org/10.1021/acs.chemrev.0c00385.

[25] H. Vanda, Y. Dai, E.G. Wilson, R. Verpoorte, Y.H. Choi, Green solvents from ionic liquids and deep eutectic solvents to natural deep eutectic solvents, C. R. Chim. 21 (2018) 628–638, https://doi.org/10.1016/j.crci.2018.04.002.

[26] Y. Chen, T. Mu, Revisiting greenness of ionic liquids and deep eutectic solvents, Green, Chem. Eng. 2 (2021) 174–186, https://doi.org/10.1016/j.gce.2021.01.004.

[27] K.S. Khoo, K.W. Chew, G.Y. Yew, S. Manickam, C.W. Ooi, P.L. Show, Integrated ultrasound-assisted liquid biphasic flotation for efficient extraction of astaxanthin from Haematococcus pluvialis, Ultrason. Sonochem. 67 (2020) 105052, https://doi.org/10.1016/J.ULTSONCH.2020.105052.

[28] C.U. Mussagy, V.C. Santos-Ebinuma, R.D. Herculano, J.A.P. Coutinho, J.F.B. Pereira, A. Pessoa, Ionic liquids or eutectic solvents? Identifying the best solvents for the extraction of astaxanthin and β-carotene from *Phaffia rhodozyma* yeast and preparation of biodegradable films, Green Chem. 24 (2022) 118–123. DOI: 10.1039/D1GC03521E.

[29] F. Caré, D. Sangaré, S. Bostyn, S. Atwi-Ghaddar, P. Lafite, F. Buron, Computational Fluid Dynamics (CFD) modeling of static maceration in view to optimize continuous flow extractions of robinetin and dihydrorobinetin from Robinia pseudoacacia wood, Food Bioprod. Process. 141 (2023) 185–198, https://doi.org/10.1016/j.fbp.2023.07.007.

[30] D. Sangare, S. Bostyn, M. Moscosa-Santillan, I. Gökalp, Hydrodynamics, heat transfer and kinetics reaction of CFD modeling of a batch stirred reactor under hydrothermal carbonization conditions, Energy 219 (2021) 119635, https://doi.org/10.1016/j.energy.2020.119635.

[31] Y. Kokubo, Frequency range dependent TE $_{10}$ to TE $_{20}$ mode converter, Microw. Opt. Technol. Lett. 52 (2010) 169–171, https://doi.org/10.1002/mop.24886.

[32] J.R. Arballo, S.M. Goñi, R.H. Mascheroni, Modeling of fluid dynamics and water vapor transport in microwave ovens, Food Bioprod. Process. 119 (2020) 75–87, https://doi.org/10.1016/j.fbp.2019.10.015.

[33] A.K. Datta, V. Rakesh, Principles of Microwave Combination Heating, Compr Rev Food Sci Food Saf 12 (2013) 24–39, https://doi.org/10.1111/j.1541-4337.2012.00211.x.

[34] J. Chen, K. Pitchai, S. Birla, M. Negahban, D. Jones, J. Subbiah, Heat and Mass Transport during Microwave Heating of Mashed Potato in Domestic Oven—Model Development, Validation, and Sensitivity Analysis, J. Food Sci 79 (2014), https://doi.org/10.1111/1750-3841.12636.

[35] P. Verboven, A.K. Datta, N.T. Anh, N. Scheerlinck, B.M. Nicolaï, Computation of airflow effects on heat and mass transfer in a microwave oven, J. Food Eng 59 (2003) 181–190, https://doi.org/10.1016/S0260-8774(02)00456-9.

[36] C.R. Wilke, P. Chang, Correlation of diffusion coefficients in dilute solutions, AIChE J 1 (1955) 264–270, https://doi.org/10.1002/aic.690010222.

[37] A.L. Sazali, N. AlMasoud, S.K. Amran, T.S. Alomar, K.F. Pa'ee, Z.M. El-Bahy, T.-L. K. Yong, D.J. Dailin, L.F. Chuah, Physicochemical and thermal characteristics of choline chloride-based deep eutectic solvents, Chemosphere 338 (2023) 139485, https://doi.org/10.1016/j.chemosphere.2023.139485.

[38] D. Sangaré, F. Caré, F. Buron, P. Lafite, S. Bostyn, Numerical modeling and evaluation of solid-liquid extraction with pressurized hot water extraction applied to Robinia Pseudoacacia wood, Chem. Eng. Process. - Process Intesif. 195 (2024) 109605, https://doi.org/10.1016/j.cep.2023.109605.

[39] N. Delgado, M. Olivera, F. Cádiz, G. Bravo, I. Montenegro, A. Madrid, C. Fuentealba, R. Pedreschi, E. Salgado, X. Besoain, Volatile Organic Compounds (VOCs) Produced by Gluconobacter cerinus and Hanseniaspora osmophila Displaying Control Effect against Table Grape-Rot Pathogens, Antibiotics 10 (2021) 663, https://doi.org/10.3390/antibiotics10060663.

[40] J. Guajardo, S. Saa, N. Riquelme, G. Browne, C. Youlton, M. Castro, X. Besoain, Characterization of Oomycete Species Associated With Root and Crown Rot of English Walnut in Chile, Plant Dis. 103 (2019) 691–696, https://doi.org/10.1094/PDIS-07-18-1160-RE.

[41] W.E. Baethgen, M.M. Alley, A manual colorimetric procedure for measuring ammonium nitrogen in soil and plant Kjeldahl digests, Commun Soil Sci Plant Anal 20 (1989) 961–969, https://doi.org/10.1080/00103628909368129.

[42] D. Berríos, P. Fincheira, F. González, C. Santander, P. Cornejo, A. Ruiz, Impact of Sodium Alginate-Encapsulated Iron Nanoparticles and Soil Yeasts on the Photosynthesis Performance of Lactuca sativa L, Plants, Plants 13 (2024) 2042, https://doi.org/10.3390/plants13152042.

[43] S. Petrasch, S.J. Knapp, J.A.L. van Kan, B. Blanco-Ulate, Grey mould of strawberry, a devastating disease caused by the ubiquitous necrotrophic fungal pathogen *Botrytis cinerea*, Mol. Plant Pathol 20 (2019) 877–892, https://doi.org/10.1111/mpp.12794.

[44] A.R. Hardham, L.M. Blackman, Phytophthora cinnamomi, Mol. Plant Pathol 19 (2018) 260–285, https://doi.org/10.1111/mpp.12568.

[45] K. Sartaj, P. Gupta, S. Tripathi, K.M. Poluri, R. Prasad, Insights into the extraction, characterization and antifungal activity of astaxanthin derived from yeast de-oiled biomass, Environ. Technol Innov 27 (2022) 102437, https://doi.org/10.1016/j.eti.2022.102437.

[46] V. Bušić, S. Roca, D. Vikić-Topić, K. Vrandečić, J. Ćosić, M. Molnar, D. Gašo-Sokač, Eco-friendly quaternization of nicotinamide and 2-bromoacetophenones in deep eutectic solvents Antifungal activity of the products, Environ. Chem. Lett. 18 (2020) 889–894, https://doi.org/10.1007/s10311-020-00973-3.

[47] A. Seguel, J. Cumming, P. Cornejo, F. Borie, Aluminum tolerance of wheat cultivars and relation to arbuscular mycorrhizal colonization in a non-limed and limed Andisol, Appl. Soil Ecol. 108 (2016) 228–237, https://doi.org/10.1016/j.apsoil.2016.08.014.

[48] P. Cornejo, R. Rubio, C. Castillo, R. Azcón, F. Borie, Mycorrhizal effectiveness on wheat nutrient acquisition in an acidic soil from southern chile as affected by nitrogen sources, J. Plant Nutr. 31 (2008) 1555–1569, https://doi.org/10.1080/01904160802244670.

[49] F. Borie, P. Aguilera, C. Castillo, A. Valentine, A. Seguel, J.M. Barea, P. Cornejo, Revisiting the nature of phosphorus pools in chilean volcanic soils as a basis for arbuscular mycorrhizal management in plant p acquisition, J. Soil Sci. Plant Nutr. 19 (2019) 390–401, https://doi.org/10.1007/s42729-019-00041-y.

[50] C. Vidal, F. González, C. Santander, R. Pérez, V. Gallardo, C. Santos, H. Aponte, A. Ruiz, P. Cornejo, Management of rhizosphere microbiota and plant production under drought stress: a comprehensive review, Plants 11 (2022) 2437, https://doi.org/10.3390/plants11182437.